Optical Engineering

SPIEDigitalLibrary.org/oe

In-flight aero-optics of turrets

Nicholas De Lucca
Stanislav Gordeyev
Eric Jumper

Optical Engineering 52(7), 071405 (July 2013)

In-flight aero-optics of turrets

Nicholas De Lucca
Stanislav Gordeyev
Eric Jumper
University of Notre Dame
Hessert Laboratory
Notre Dame, Indiana 46556
E-mail: ndelucca@nd.edu

Abstract. Recent in-flight aero-optical measurements from the Airborne Aero-Optics Laboratory are provided, along with instrumentation and experimental set-up. Results of an extensive survey of the aero-optical environment at different viewing angles, for both flat-window and conformal-window turrets at different subsonic and low transonic speeds below $M = 0.65$, are presented, compared and extensively discussed. A comparison between two turret geometries, hemisphere-on-cylinder and hemisphere only, plus the statistical analysis of wavefronts at different viewing angles, are also presented and discussed. Additionally, dynamics of a local shock appearing on the conformal-window turret at transonic Mach number are discussed. [DOI: 10.1117/1.OE.52.7.071405]

Subject terms: aero-optics; turrets; Airborne Aero-Optics Laboratory; wavefronts; flight tests.

Paper 121437SSP received Oct. 1, 2012; revised manuscript received Nov. 14, 2012; accepted for publication Nov. 20, 2012; published online Jan. 31, 2013.

1 Introduction

Several flight platforms for laser systems have been developed over the years, from the Airborne Laser Laboratory (ALL) in the 1970s to the Airborne Tactical Laser (ATL) in the 2000s. A common feature of laser projection systems is the hemisphere-on-cylinder turret, a geometry that from a diffraction-limited point of view provides an excellent field of regard, but introduces several unique aero-optical problems[1] when used in typical flows around aircraft.[2] As shown in Fig. 1, the upstream portion of the flow field around the turret is relatively benign; the curvature of the turret induces a favorable pressure gradient that keeps the flow attached. The curvature of the downstream portion of the turret has an opposite effect—an adverse pressure gradient forms that leads to flow separation and the formulation of a highly turbulent wake. This wake creates a fluctuating density field that gives rise to an index-of-refraction variation in the air. The vortical structures in the wake include two horn vortices. About the base of the cylinder, a necklace vortex forms and propagates downstream. These flow features are dependent on the Reynolds number until a minimum Reynolds number is reached. Additionally, for incoming Mach numbers larger than 0.55, a shock forms over the top of the turret as the flow becomes locally supersonic.[2,3]

In addition to aero-optical effects, the unsteady pressure field of the flow induces mechanical vibration in the turret that may result in a significant beam jitter. These two effects can significantly reduce the far field intensity of the laser and limit the effective field of regard for the turret.

The turret viewing direction is commonly described with two angles, the azimuthal angle (Az) and the elevation angle (El). From a fluid-flow perspective, a different coordinate system helps to collapse the data and still be able to account for some El dependence. As shown in Fig. 1(b), the azimuth and Els are transformed into two new angles, α, the viewing angle and β, the modified El. The transformation for these two angles is given by $\alpha = \cos^{-1}[\cos(\mathrm{Az})\cos(\mathrm{El})]$ and $\beta = \tan^{-1}[\frac{\tan(\mathrm{El})}{\sin(\mathrm{Az})}]$. The reason for this coordinate change can be demonstrated using the turret flow field described in Fig. 1. For pure spheres, the flow field would only be a function of how far upstream or downstream the turret is looking, which is represented by the angle α. The modified El accounts for changes in the flow that are derived from the symmetry-breaking presence of the cylinder under the hemisphere, the aircraft wall and the existence of the horn vortices mentioned earlier.

0091-3286/2013/$25.00 © 2013 SPIE

2 Experimental Setup

2.1 *Instrumentation*

The Airborne Aero-Optics Laboratory (AAOL) provides a flight-test platform for studying these and other aero-optical effects and designing mitigation systems with flow control or adaptive optics. Detailed description of AAOL is provided in Jumper et al.[4] Here we provide only the essential details about the flight experiment. Two aircraft flying in closed formation, approximately 50 m apart, are used in the AAOL program. The laboratory aircraft holds the turret assembly, mounted to the optical bench inside the aircraft so that it protrudes into the airstream through a modified escape hatch. The various other measurement systems can also be integrated into the escape hatch. The second aircraft projects a laser beam onto the laboratory aircraft turret pupil. This source laser is projected out of a window on the source aircraft, instead from a second turret, to minimize aero-optical distortions on the outgoing beam. The emitted laser projects through the attached boundary layer as a small beam aperture that is diverging so that by the time it arrives at the laboratory turret it overfills the turret pupil by a factor of two. Because of the initial small beam size and overfill of the laboratory aircraft turret pupil, the tracking requirements for the source beam are somewhat less than that for the turret on the laboratory aircraft. Images of the turret with both flat and conformal apertures are given in Fig. 2.

An annotated photograph and schematics of the optical bench on the laboratory aircraft are given in Fig. 3. The primary sensor on the laboratory aircraft (AAOL) is the

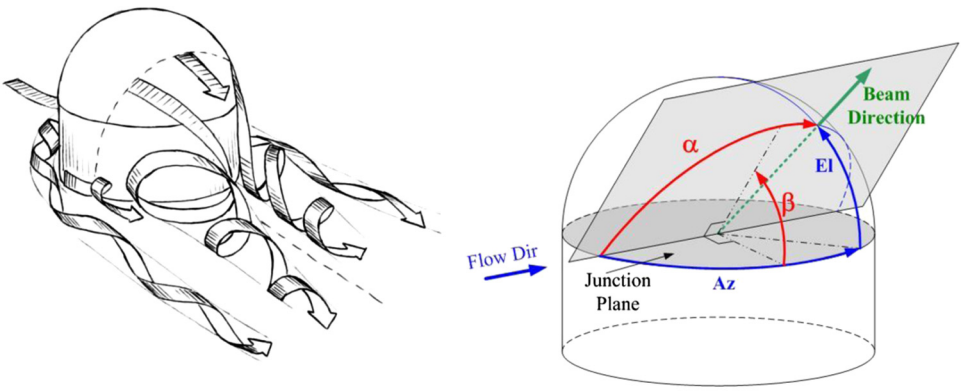

Fig. 1 The dominant flow structures around a hemisphere-on-cylinder turret (a) and the turret viewing angle definitions (b).

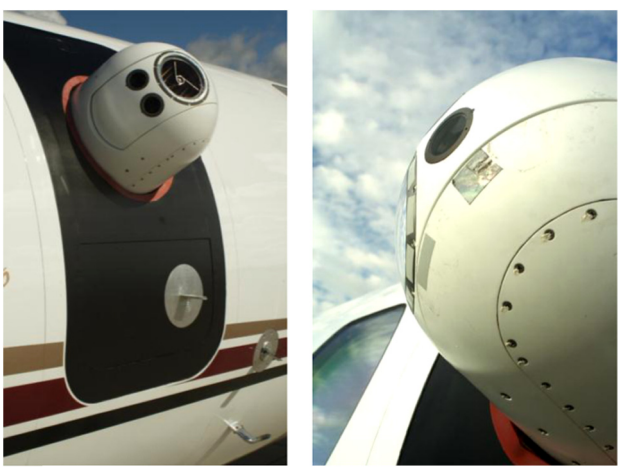

Fig. 2 The AAOL turret with a flat-window (a) and a conformal-window (b) apertures.

high-speed two-dimensional (2-D) Shack-Hartmann wavefront (WF) sensor, capable of acquiring wavefronts with spatial resolution of 32×32 at 25 kHz. The initial 0.10 m aperture beam is re-imaged to the 0.02 m beam. Additionally, the turret assembly contains a closed-loop fast steering mirror (FSM) system which stabilizes the beam on the sensor. Residual beam jitter is measured by a position sensing device (PSD) on the optical table. In addition to acquiring WFs and the residual jitter, instantaneous flight speed, static/total pressures and the turret's elevation and azimuth angles were recorded, along with the instantaneous distance between the two aircraft measured via differential global positioning system (GPS). The residual jitter data, flight parameters and turret angles were acquired simultaneously at 100 kHz. The WFs and GPS data were collected with separate data acquisition systems at different sampling speeds, but they were synchronized with the jitter data. Although it was acquired during flight tests, the residual jitter and GPS data will not be discussed in this paper. The analysis of the jitter data can be found in the companion paper.[5]

Data were acquired in one of two different modes: a fixed relative aircraft position or a "slew" maneuver. For fixed-position data, WFs were acquired at 25 kHz for 15,000 frames. Fixed position data allows collected data at higher sampling frequency for a better time resolution of aero-optical structures. A slewing maneuver involved the source laser aircraft moving slowly and monotonically with respect to the turret aircraft. To enable data acquisition for a longer time period of 7 s, the WF acquisition rate was reduced to 3 kHz for slewing maneuvers and a total of 21,000 WFs were acquired per each slew maneuver. WFs collected during slewing maneuvers, while not time-resolved, provided statistical properties of aero-optical distortions over a range of elevation/azimuthal angles and facilitate an overall mapping of the optical performance of the turret over a large field of regard. Flight conditions varied from $M = 0.4$ or $M = 0.5$ at an altitude of 15,000 ft to $M = 0.6$–0.65 at altitudes from 28,000 to 34,000 ft.

2.2 *WF Reduction and Analysis*

Processing image data from the high-speed WF sensor provides spatial-temporal-resolved WF sequences, $W = W(x, y, t)$. For each WF sequence, the steady lensing, instantaneous tip/tilt and instantaneous piston were removed from each WF during data reduction. The procedure is slightly different for slewing maneuvers, as will be explained here in more detail later. The optical path difference (OPD), which is the conjugate of the WF, is given by $\mathrm{OPD} = -W$. Several statistical quantities were calculated from these WF sequences. One of them is the instantaneous spatial root mean square (RMS) of the OPD over the aperture, $\mathrm{OPD}_{\mathrm{RMS}}(t) = \sqrt{\langle \mathrm{OPD}(x, y, t)^2 \rangle_{x,y}}$, where angle brackets denote spatial averaging over the aperture. The time-averaged $\mathrm{OPD}_{\mathrm{RMS}}(t)$, later in this paper denoted by just $\mathrm{OPD}_{\mathrm{RMS}}$, gives the overall value of aero-optical distortions at a given angle. The temporal histogram of instantaneous $\mathrm{OPD}_{\mathrm{RMS}}(t)$ provides useful information about the temporal deviation around the time-averaged $\mathrm{OPD}_{\mathrm{RMS}}$ and is also useful for checking data quality. The temporal variation of $\mathrm{OPD}_{\mathrm{RMS}}(t)$ is quantified by the spread of the $\mathrm{OPD}_{\mathrm{RMS}}(t)$, defined as $\Sigma = \sqrt{\overline{[\mathrm{OPD}_{\mathrm{RMS}}(t) - \overline{\mathrm{OPD}_{\mathrm{RMS}}}]^2}}$, which is the standard deviation of the $\mathrm{OPD}_{\mathrm{RMS}}$ over its time-averaged value. It is also useful to quantify the spatial distribution of the aero-optical distortions. This is achieved by taking the temporal RMS of the OPD of each fixed point over the aperture, $\mathrm{OPD}_{\mathrm{RMS}}(x, y) = \sqrt{\overline{\mathrm{OPD}(x, y, t)^2}}$,

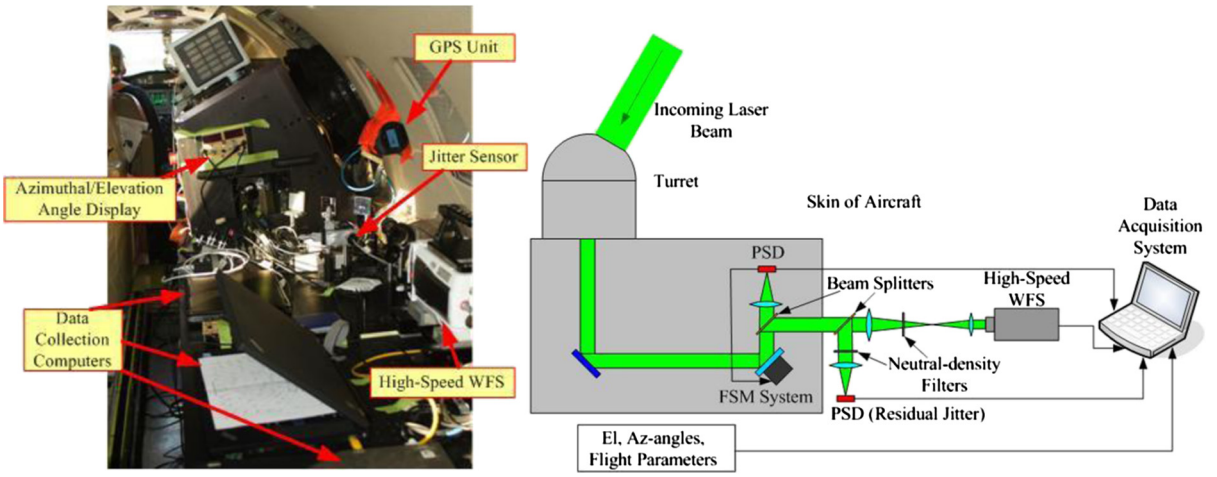

Fig. 3 The optical setup on the turret aircraft.

later referred to in this paper as the spatial distribution of OPD_{RMS}.

Before raw images from the high-speed WF sensor were converted into WFs, WF data quality was checked through several measures. The first series of checks occurs during WF data reduction. In Fig. 4 an example of a raw image file is presented; it should be noted that this image has been image enhanced so that it is easier to view. Although the Shack-Hartmann sensor is technically intensity-invariant, the intensity of a given dot can vary in time, potentially affecting the data quality. As a result, any location on the image with sufficiently low-intensity can temporally lose enough intensity to make centroid determination inaccurate. To correct for this, dots with very low average intensity were ignored in processing. Additionally, having intensity that is too large will saturate the dot image and reduce the subpixel resolution for centroid determination. To avoid this issue, neutral-density filters were, if needed, added to or removed from the optical train in flight to regulate the beam intensity at the sensor.

The mean flow around the turret imposes a density field that lenses the beam. This steady lensing is viewing-angle and elevation-angle dependent. Because the beam train assumes a specific aircraft separation when re-imaging, the steady lensing also has a defocus component, depending on the relative distance between the two aircraft. The strength of this defocus changes over the course of a slew maneuver as aircraft separation does not remain constant. The total steady lensing of the beam is removed for each averaging subset to compensate for both these effects. To eliminate this corrupting effect during a slew maneuver, the slew data series were split into 0.5-s subsets, and average statistics were computed over the these subset time periods; thus, the short-time steady lensing and the instantaneous tip/tilt were removed from each 0.5-s subset. The slew rate for the aircraft, in terms of turret rotation, was typically 2 deg per second, and as a result, averaging over a half second of data gave results in averaging over a single degree of rotation. Figure 5 shows the statistical convergence of OPD_{RMS} as a function of data set duration. The OPD_{RMS} converges within half a second, confirming that 0.5-s data sequence provides correct statistics of OPD_{RMS} at the viewing angle. As fixed-position data were acquired at 25 kHz for 0.6 s, it was not subdivided and the steady lensing across all frames and instantaneous tip/tilt were removed. The full suite of statistics

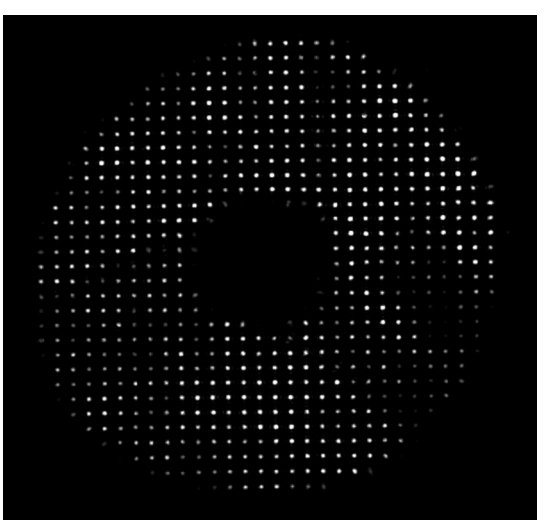

Fig. 4 A sample image from the Shack-Hartmann WF sensor.

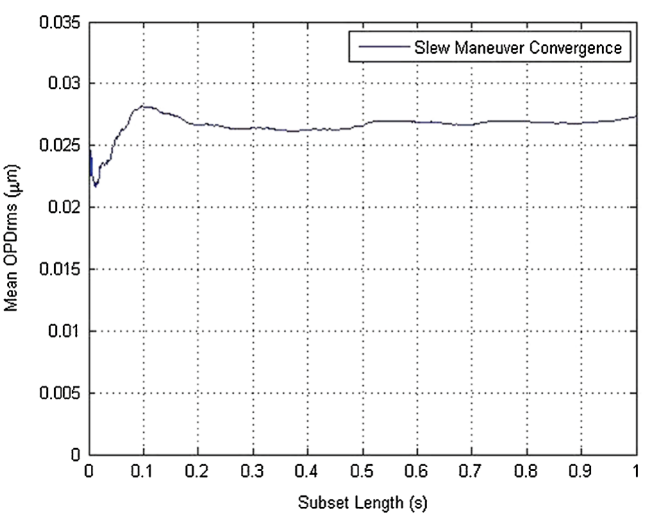

Fig. 5 The convergence of OPD_{RMS} for a slew maneuver.

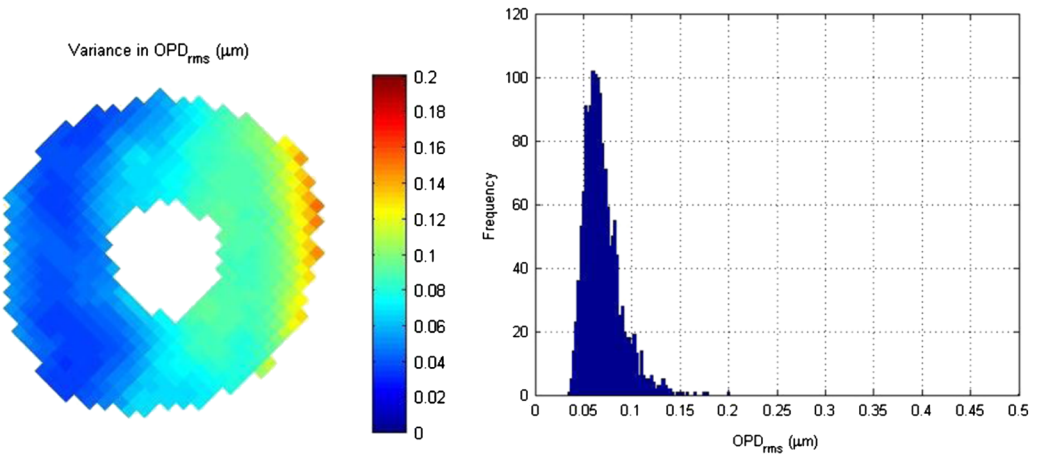

Fig. 6 Sample spatial distribution of OPD_{RMS} and histogram of OPD_{RMS} over the aperture. $M = 0.48$, $\alpha = 106$ deg, $\beta = 62.2$ deg.

was computed for each fixed-angle data set and each slewing maneuver subset.

After images from the high-speed WF sensor were converted into WF sequences, using either commercially available or in-house-developed software, various statistical quantities were calculated from them, as discussed earlier. Besides providing important statistical information about aero-optical distortions, these quantities give additional measures of data quality. Figure 6 gives an example of two metrics, the spatial distribution of OPD_{RMS} and probability distribution function of the instantaneous OPD_{RMS}. For the spatial distribution of the OPD_{RMS} at back-looking angles, the linear gradient in the flow direction is typical of a shear layer formed over the aperture; the downstream portion of the aperture looks through a larger portion of the shear layer than the upstream part, increasing the local OPD_{RMS}. The spatial distribution also does not contain any obvious modes such as a large defocus contribution or any single points that are vastly different from those near it. The histograms of the temporal distribution of OPD_{RMS} typically have a log-normal distribution, as shown in Fig. 6, right plot. WFs with unusually large values of OPD_{RMS} will be present in the histogram as a number of outliers in the distribution tail, which might indicate that these WFs are corrupted.

3 Results

3.1 *Subsonic Flight Data*

To compare the aero-optical environment between flat and conformal turret windows, OPD_{rms} was computed at a large number of azimuth and Els. The OPD_{RMS} values were normalized by flight conditions,

$$\mathrm{OPD}_{\mathrm{Norm}}\left(\frac{\mu m}{m}\right) = \frac{\mathrm{OPD}_{\mathrm{RMS}}}{\left(\frac{\rho}{\rho_{\mathrm{SL}}}\right)M^2 D}.$$

Here the free stream density is ρ, while the density at sea level is ρ_{SL}. The diameter of the turret is given by D and M is the free stream Mach number. This scaling was previously shown to correctly normalize aero-optical distortions over turrets for subsonic Mach numbers of 0.4 to 0.5.[6]

The OPD_{RMS} for the full turret is mapped out in Fig. 7. The top plots demonstrate the mapping in the traditional azimuthal angle and El coordinate system, while the bottom plots transform the mapping into viewing angle and modified El space. Figure 8 contains the mapping in just viewing angle space for the hemisphere-only turret. For all of the mappings contained in the paper, color features are linearly interpolated between actual data points, given by the gray dots, and as a result, some features in data-sparse areas may be artifacts of the interpolation. To better understand the way these maps represent the optical performance of the turret and related flow features, Fig. 9 splits this data into several bands of the modified El, β, 30 to 50 deg, 50 to 70 deg, 70 to 80 deg, and 80 to 90 deg, which are shown in Figs. 7 and 8 as green lines.

Analysis will begin with the flat window, located on the left sides of Figs. 7 and 8 and in Fig. 9. For $\alpha < 80$ deg, the aero-optical environment on the full turret is relatively inert, with normalized $OPD_{RMS} < 1.5$. The aero-optical environment in this range at short timescales, in the order of a millisecond, is dominated by turbulent structures in the boundary layer over the flat window.[7,8] For longer timescales, in the order of $St_D = fD/U_\infty \sim 0.2 \ldots 0.4$ or in tens of milliseconds, a time-changing defocus is present.[9] This relatively slow time-varying defocus is due to the presence of the necklace vortex and turbulent wake that induce changes in the global pressure field that result in local density fluctuation over the aperture. As the data presented in Figs. 7 and 8 are averaged over 0.5 s to remove defocus due to changing aircraft separation, this aero-optical unsteady defocus in the forward field is kept in WFs. As α decreases, OPD_{RMS} also decreases as the turret is looking through a thinner boundary layer closer to the upstream edge of the turret, an effect seen in boundary-layer aero-optical studies.[7,8] The hemisphere-only turret in this regime has a thinner boundary layer compared to the full turret, as shown by reduced OPD_{RMS} values for $\alpha < 80$ deg. For 80 deg $< \alpha <$ 110 deg, the slope discontinuity of the flat window generates a separation bubble that resides over the flat window. This separation bubble continues to grow as α increases. OPD_{RMS}, however, peaks at a value dependent on β and then decreases. This effect is due to the tip/tilt removal of the WFs, and has been studied previously in Ref. 10. The β dependence is due to the presence of the necklace vortex near the wall of the aircraft influencing the dynamics of the small separation bubble via Biot-Savart induction mechanism. The

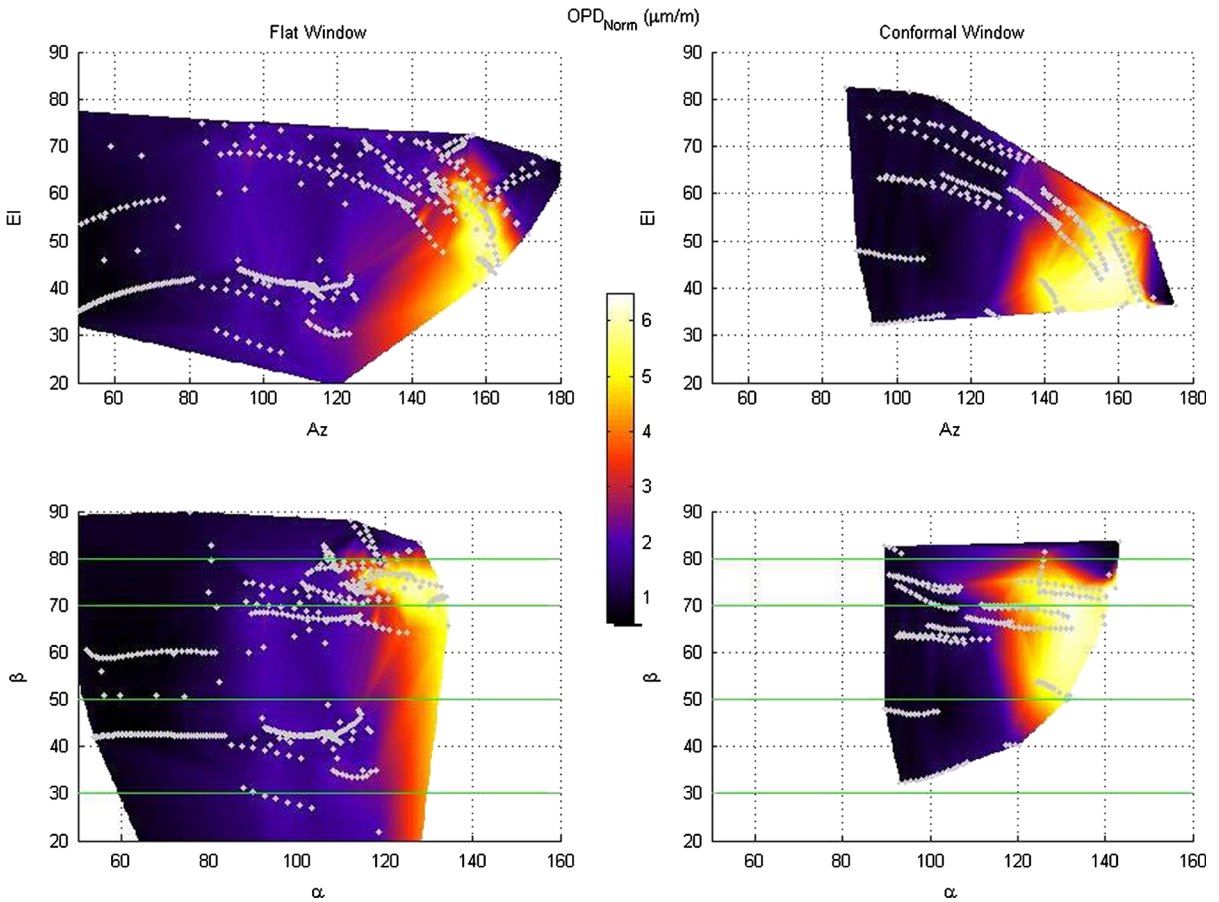

Fig. 7 Maps of OPD_{RMS} as a function of both azimuth and elevation angles and viewing and modified elevation angles frame-of-references for the full hemisphere-on-cylinder turret in subsonic flow.

general behavior of this peak is that it occurs at smaller α as β increases. The same effect is seen in on the hemisphere-only turret, with similar OPD_{RMS} values to the full turret. The dependence of this flow feature solely on the local geometry is the reason for this similarity. However, just as the location of this peak is dependent on β, it also is impacted by turret height for the same reason, and the peak locations vary between the two turret geometries. For $\alpha > 110$ to 120 deg, the flow begins to separate into a fully turbulent wake. The exact separation point is dependent on β, with separation occurring at smaller α for larger β. Comparing the hemisphere-on-cylinder turret to the hemisphere-only turret, separation occurs at approximately the same location, but OPD_{RMS} values in the wake are somewhat lower for the

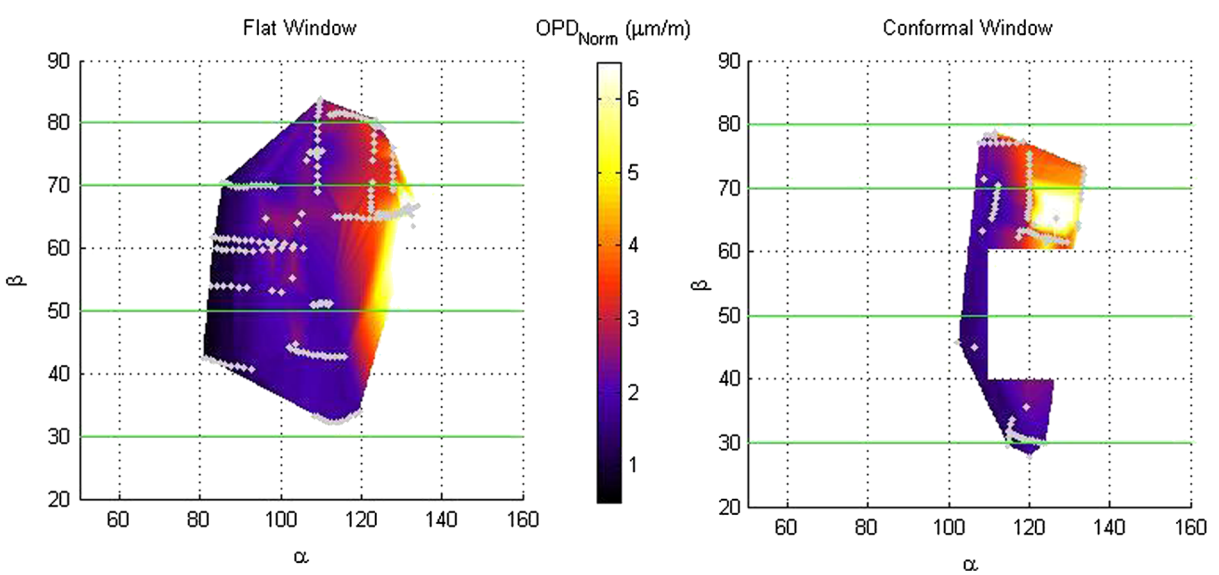

Fig. 8 Maps of OPD_{RMS} as a function of viewing and modified elevation angles for the hemisphere-only turret in subsonic flow.

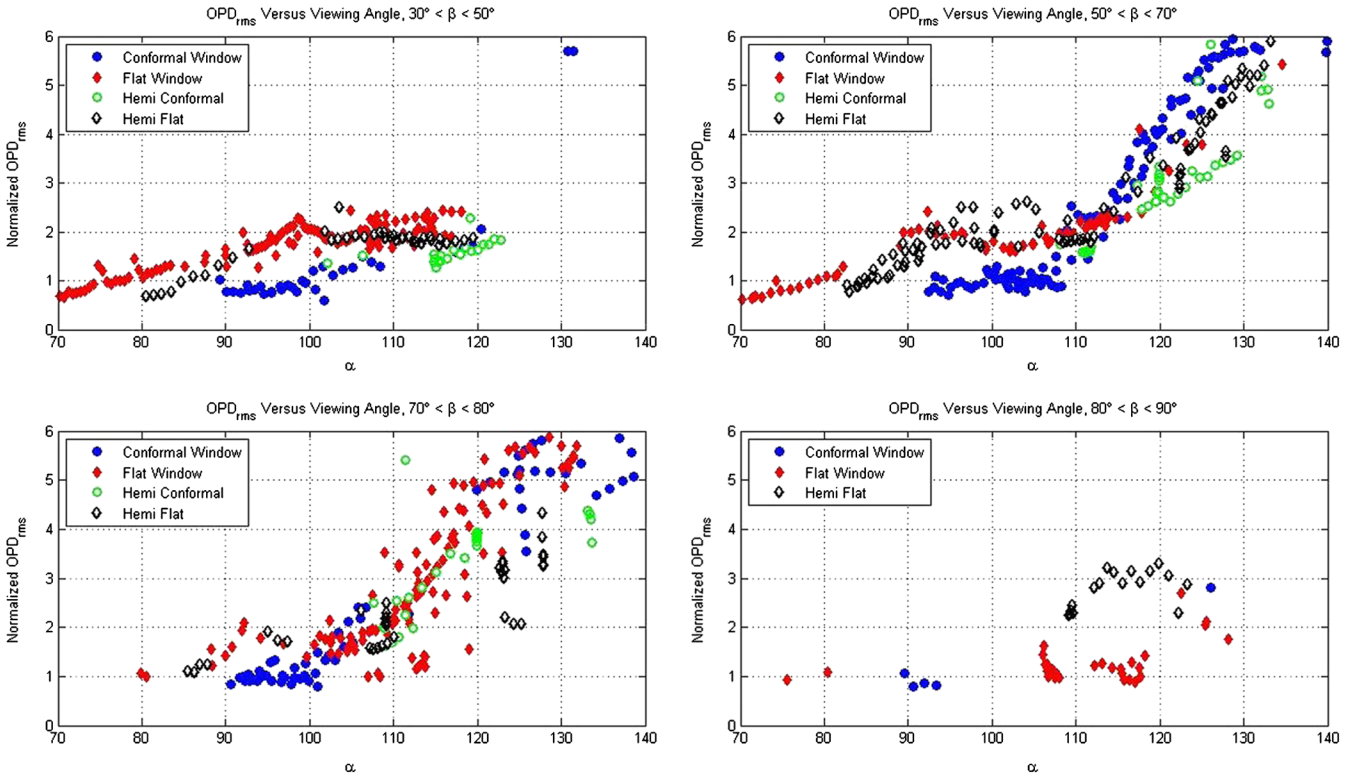

Fig. 9 OPD_{RMS} versus viewing angle, broken into bands of modified elevation angle for subsonic flow.

hemisphere-only turret, as the reduced profile of the turret results in a smaller wake, which reduces OPD_{RMS} values. The exception to this occurs for $\beta > 80$ deg. In this regime, the full turret is looking directly between the two horn vortices of the wake, and OPD_{RMS} is reduced as a result. With the smaller profile turret, the horn vortices are closer to the window, resulting in an increase the OPD_{RMS} compared to the full turret. Similar results along the center plane were observed previously.[2]

The conformal window exhibits many of the same behaviors as the flat window, with the main difference being that the conformal-window does not form the local separation bubble over the aperture. For this analysis, we will refer to right plots in Figs. 7–9. The $\alpha < 110$ deg range for the conformal window is mostly dominated by the attached turbulent boundary layer. In this range, OPD_{RMS} values are always lower than for the flat window turret. However, the separation point for the conformal-window turret occurs at a slightly smaller α than for the flat-window turret. To explain this, recall that the separation occurs as adverse pressure gradient forms over the turret. This adverse pressure gradient is a function of the curvature of the turret. The strength of the adverse pressure gradient is related to the slope of the surface of the turret. For a flat window, the slope is constant over the window, and the magnitude of the adverse pressure gradient is constant as well. For the conformal window, the curvature means that even though the slope of the window is the same as the flat window at the center of the aperture, for a given $\alpha > 90$ deg, the slope becomes larger downstream of the center. The adverse pressure gradient increases towards the downstream edge of the window. The overall result of this is that increasing-strength adverse pressure gradient that forms over the conformal window forces separation to occur earlier as compared to the flat window. In the separated wake region, OPD_{RMS} values are lower with the hemisphere-only turret due to the smaller wake.

3.2 *Transonic Flight Data*

Transonic flow, in regard to optical turret, refers to free-stream Mach numbers larger than 0.55, where the flow near the apex of the turret reaches sonic and supersonic speeds.[10] In this regime, a local supersonic region with an ending shock forms on the turret and impact overall optical performance. Figure 10 shows the OPD_{RMS} maps for the transonic regime with a hemisphere-on-cylinder turret. The OPD_{RMS} maps for the hemisphere-only turret are given in Fig. 11. As before, the maps of data are broken into same bands of β, as for the subsonic case, to aid in understanding of the different flow features.

Beginning again with the flat window, there are several common features between the transonic and subsonic flow regimes. The flat window transonic data is given in Figs. 10, 11 left, and Fig. 12. For 85 deg $< \alpha <$ 110 deg and $\beta <$ 50 deg, there are increases in OPD_{RMS} compared to the subsonic case. These increases are due to a weak shock appearing near the turret apex. This occurs for both the hemisphere-on-cylinder turret and the hemisphere-only turret. The trend of flow separation occurring at smaller α as β increases continues in the transonic regime, as does that of the local maximum in the 90 deg $< \alpha <$ 110 deg range due to the separation bubble on the flat window. In the 70 deg $< \beta <$ 80 deg range, separation occurs at smaller viewing angles for the full turret at transonic speeds than subsonic speeds, and OPD_{RMS} values are elevated in the wake, indicating a larger wake at this modified El.

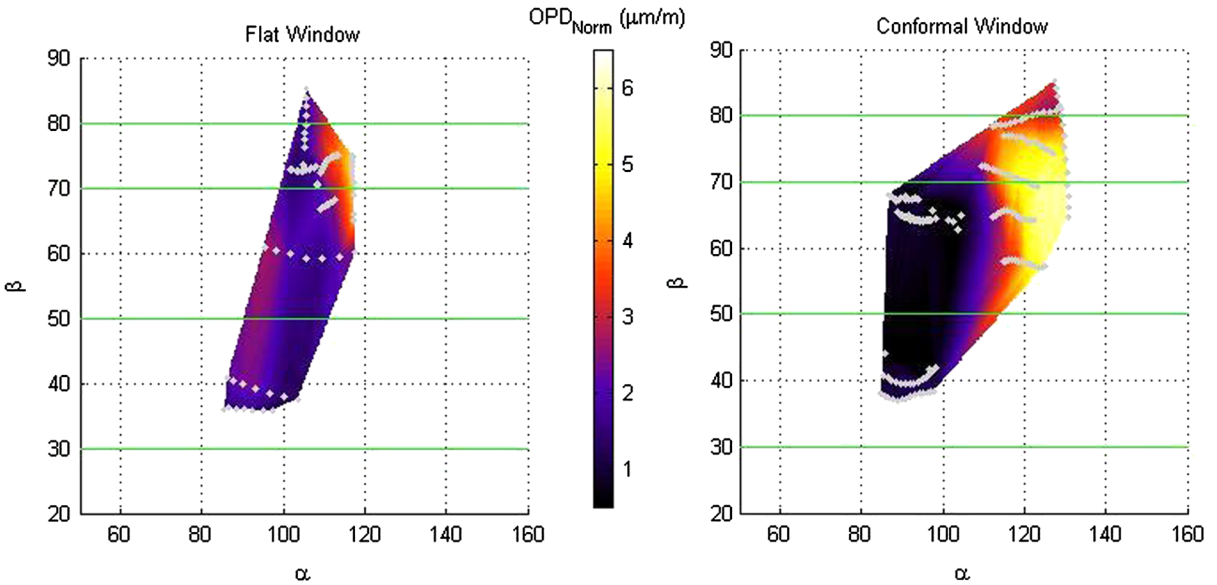

Fig. 10 Transonic OPD_{RMS} maps for the hemisphere-on-cylinder turret.

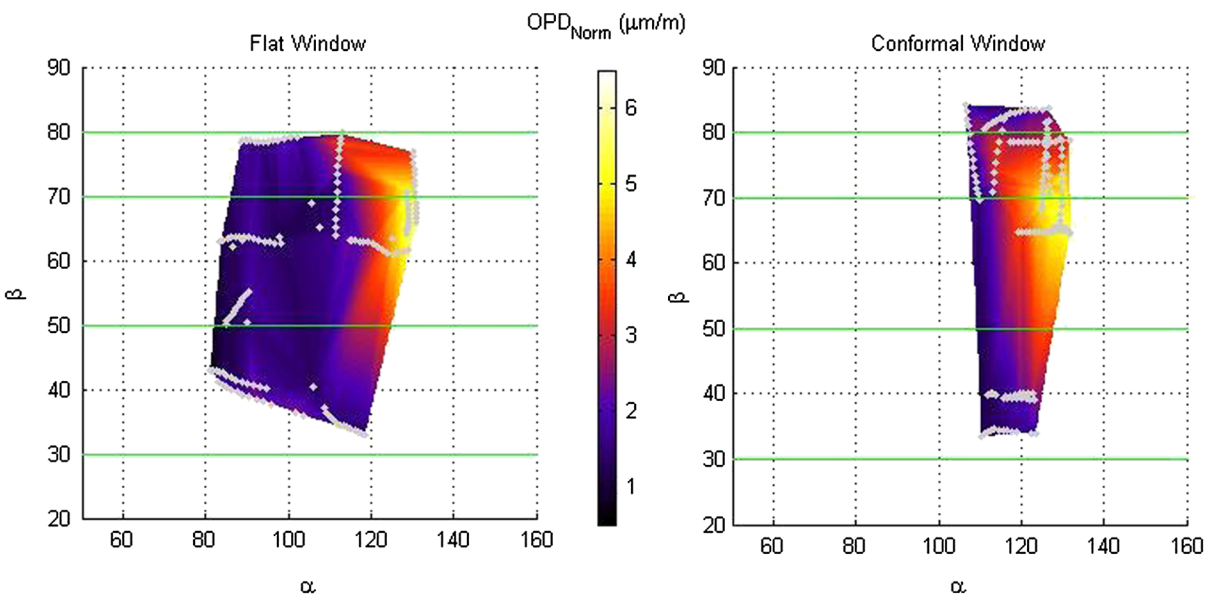

Fig. 11 Transonic OPD_{RMS} maps for the hemisphere-only turret.

The conformal turret also shows some similarities to the flat window turret at these angles, as shown in Fig. 13. For the full turret, at least, the elevation in OPD_{RMS} in the 85 deg $< \alpha <$ 100 deg region is also present with the conformal window. This increase is again due to a weak shock near the turret apex; however, the increase is less pronounced for the conformal window than for the flat window. This indicates an interaction between the flat window and the shock. In the 50 deg $< \beta <$ 70 deg range, the separation point is unchanged, but the OPD_{RMS} values in the wake are elevated slightly for the transonic flow in the full turret case, indicative of a slightly stronger wake. The same trend of lower OPD_{RMS} values for the hemisphere-only turret repeats as well. For $\beta >$ 80 deg, the reduced OPD_{RMS} values in the wake region are present. This indicates that the wake is still primarily composed of the two horn vortices in the transonic regime, and in this region the turret is still looking between them.

3.3 *Temporal Variation of OPD_{RMS} and Communications Applications*

While the time-averaged OPD_{RMS} directly affects the intensity at the target, OPD_{RMS} varies in time, as can be seen in time histogram, Fig. 6, right. In terms of system performance this is indicative of time periods when $OPD_{RMS}(t)$ is larger than the time-averaged OPD_{RMS}, resulting in a further decrease in the far-field intensity, a potentially detrimental effect to airborne laser-based communication systems.

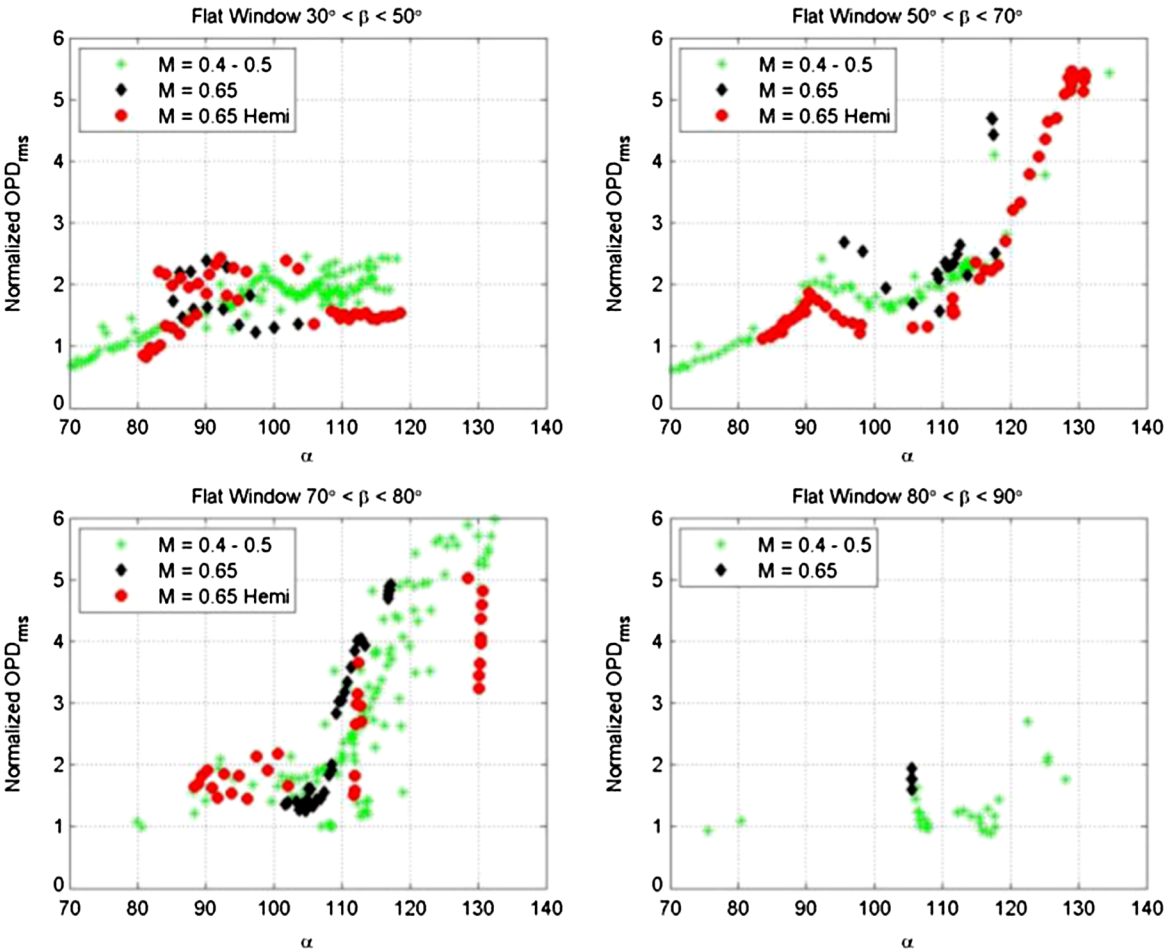

Fig. 12 $\mathrm{OPD_{RMS}}$ for bands of modified elevation angle at transonic Mach numbers with a flat window.

To quantify the temporal variation of $\mathrm{OPD_{RMS}}(t)$ about the time-averaged $\mathrm{OPD_{RMS}}$, the temporal standard deviation of the mean-removed $\mathrm{OPD_{RMS}}(t)$ or spread, β, was calculated for all time series for different elevation/azimuthal angles. Results for the conformal window turret, normalized by $(\rho/\rho_{\mathrm{SL}})M^2D$ are presented in Fig. 9, left plot, as a function of the viewing angle for the range of 50 deg $< \beta <$ 80 deg. The spread values are low for side-looking angles $\alpha < 110$ deg and rapidly increase for higher viewing angles, following the general trend for $\mathrm{OPD_{RMS}}$ values in Fig. 9, upper right. To confirm this, the spread was normalized by the time-averaged $\mathrm{OPD_{RMS}}$; these results are plotted in Fig. 14, right. Over a wide range of viewing angles the spread was found to be approximately proportional to the $\mathrm{OPD_{RMS}}$, $\Sigma \approx 0.28 \cdot \mathrm{OPD_{RMS}}$.

It was shown in Ref. 11 that if the WF is Gaussian in space, the instantaneous far-field Strehl Ratio depends only on the instantaneous $\mathrm{OPD_{RMS}}(t)$, $\mathrm{SR}(t) = \exp\{-[2\pi \mathrm{OPD_{RMS}}(t)/\lambda]^2\}$. Analysis of the spatial distributions of the WFs for both the flat-window[7] and the conformal-window turrets revealed that the WFs do have a spatial Gaussian distribution for a wide range of elevation/azimuthal angles. Thus, if the temporal distribution of $\mathrm{OPD_{RMS}}(t)$ is known, it is possible to predict the probability distribution for the far-field Strehl ratio.[12] Analysis of the temporal distribution of $\mathrm{OPD_{RMS}}$ had shown that for subsonic speeds they can be well-approximated by a log-normal distribution,

$$\mathrm{PDF}(\mathrm{OPD_{rms}}) = \frac{1}{\mathrm{OPD_{rms}} s\sqrt{2\pi}} \exp\left[-\frac{(\ln \mathrm{OPD_{rms}} - m)^2}{2s^2}\right],$$

where parameters m and s are related to time-averaged $\mu = \mathrm{OPD_{RMS}}$ and the spread, Σ, as

$$m = \log\left[\frac{\mu}{\sqrt{1 + (\Sigma/\mu)^2}}\right], \qquad s^2 = \log[1 + (\Sigma/\mu)^2].$$

For the conformal-window turret, $\Sigma \approx 0.28 \cdot \mathrm{OPD_{RMS}} = 0.28\mu$, giving $m = \log(0.96\mu)$, $s = 0.18$, and the $\mathrm{OPD_{RMS}}$-probability distribution becomes,

$$\mathrm{PDF}(\mathrm{OPD_{rms}}) = \frac{1}{0.18\sqrt{2\pi}\mathrm{OPD_{rms}}} \times \exp\left\{-\frac{[\ln \mathrm{OPD_{rms}} - \log(0.96\mu)]^2}{0.066}\right\}.$$

If the far-field intensity threshold is given, one can predict relative duration of intensity drop-outs due and potentially lost data due to temporal variation of $\mathrm{OPD_{RMS}}(t)$ for

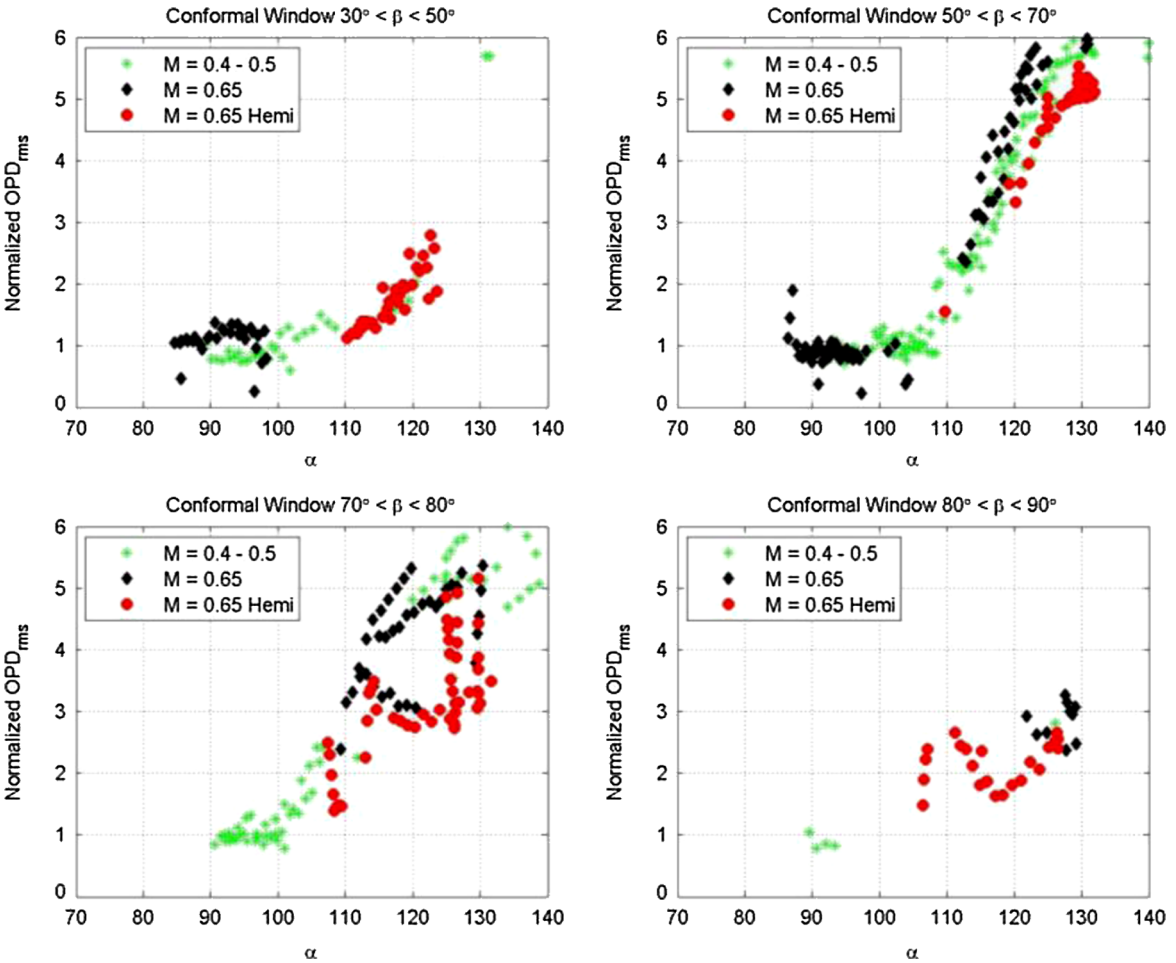

Fig. 13 OPD_{RMS} for bands of modified elevation angle at transonic Mach numbers with a conformal window.

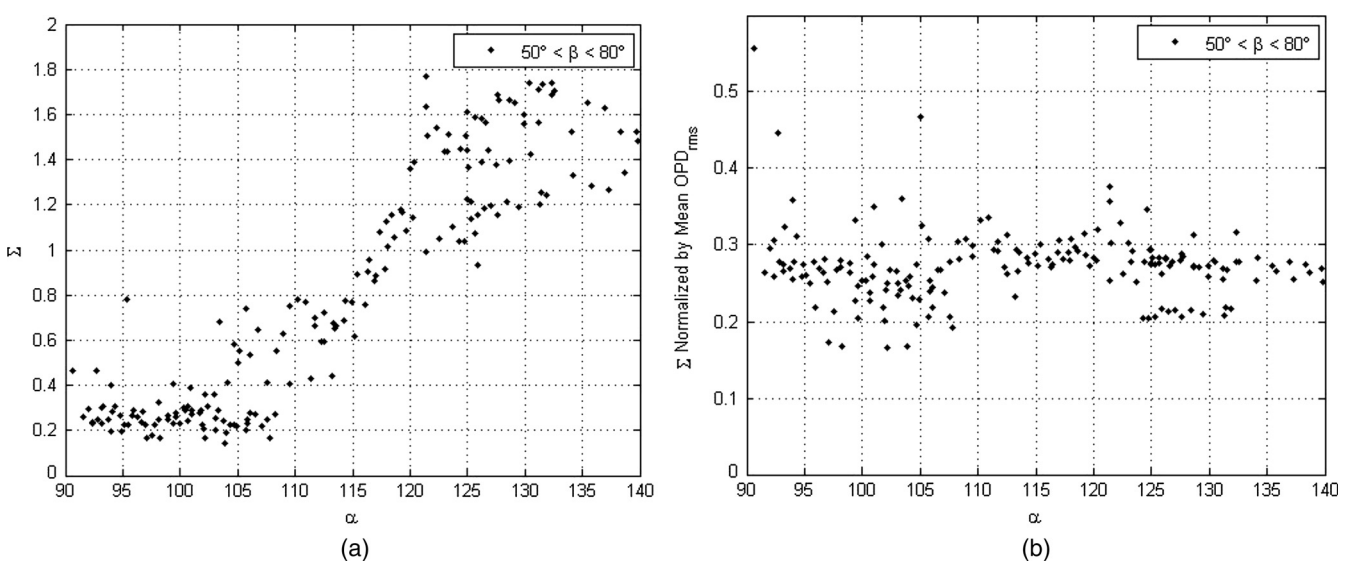

Fig. 14 (a) Temporal standard deviation of OPD_{RMS}, (b) Temporal standard deviation of OPD_{RMS} normalized by mean OPD_{RMS} for the conformal window. $M = 0.5$.

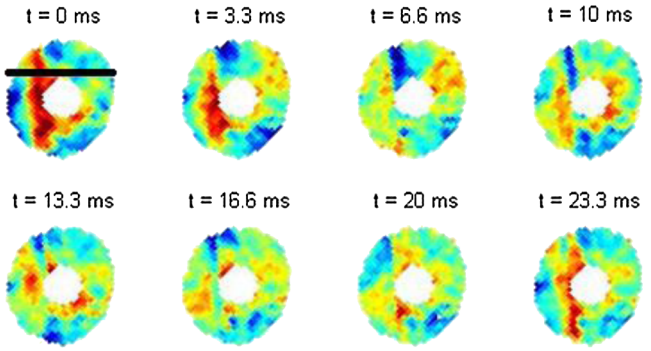

Fig. 15 Time evolution of the shock on the aperture. Conformal window turret, $M = 0.65$, $\alpha = 85$ deg, $\beta = 40$ deg. The black line, top left, shows the WF slice used for analysis.

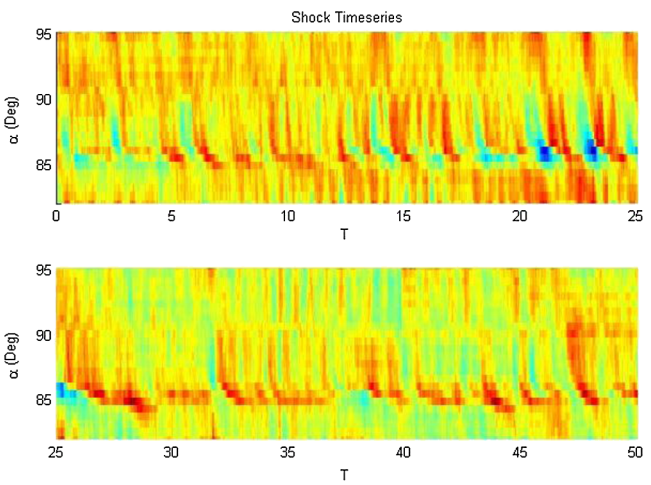

Fig. 16 Temporal evolution of one-dimensonal streamwise WFs showing the presence of intermittent shocks on top of the turret.

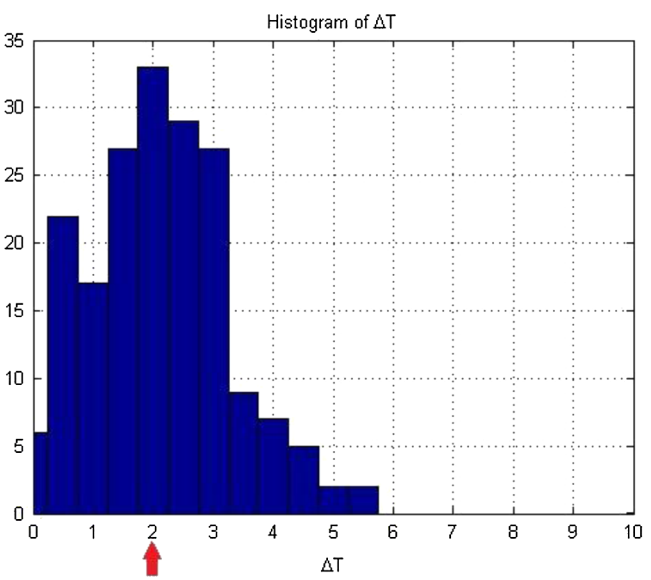

Fig. 17 Histogram of the time intervals between consecutive shock events. The most probable event at $T = 2$ is marked by an arrow.

different subsonic flight conditions and elevation/azimuthal angles.[12]

3.4 *Shock Dynamics at Transonic Speeds*

For the transonic incoming Mach number of 0.65, an intermittent shock was observed over the conformal-window aperture at approximately $\alpha = 86$ deg. Figure 15 shows several WF snapshots revealing spatio-temporal evolution of this shock; as the density experiences a jump from low values to high values across the shock, the shock is visible as a sharp gradient between the red or high values of WF and the blue or low WF.

To better understand the temporal evolution of the shock, temporal evolution of the one-dimensional (1-D) WFs were extracted along the line in the streamwise direction just outside of the obscuration region, as shown schematically in Fig. 13, $t = 0$ ms snapshot. Resulted 1-D WFs are presented in Fig. 16 as a function of the streamwise location, expressed as the viewing angle and time, normalized by the incoming speed and the turret diameter, $T = tU_\infty/D$. Shock-related events can be traced by tear-drop-like blue regions, corresponded to the low-density region just upstream of the shock around the viewing angle of 86 deg. From Fig. 16, an intermittent, yet repeatable, nature of the shock is evident. By identifying shock occurrences as time instances, where the WF locally drops to its lowest value near the viewing angle of 85 deg, we can compute time intervals between consecutive shock appearances and results are presented in Fig. 17 as a histogram. The histogram tail extends up to $\Delta T = 5.5$. The most probable time interval occurs between shock at approximately $\Delta T = 2$, and the mean time interval is $\Delta T = 2.1$. Note that POD-analysis of 2-D WF data at transonic speeds[13] revealed that shock-dominant temporal WF spectrum has a peak at normalized frequency of $fD/U_\infty = 0.5$, giving the typical (normalized) periodicity of shock events as the inverse of this value, that is $T_{\text{period}} = 2$, which is very close to the most probable time interval between shock events.

To better understand the temporal dynamics of the shock-related events, WF data were conditionally averaged in the following way: for each shock-event, identified as above, 1-D WFs were extracted between times $-1.5T$ and 1.5T, with $T = 0$ been at the shock event; WFs then were "aligned" such as each shock occurrence corresponds to $T = 0$ and then WFs were ensemble-averaged at every time and the spatial location. The conditionally averaged space-time shock-related WF is presented in Fig. 18. The shock can be seen as a sharp gradient between the blue-region below and the red-region above. To better see the shock evolution, several representative times, shown as vertical lines in Fig. 18, were selected and corresponding tilt-removed 1-D WFs at these times are plotted in Fig. 19, left plot. Also, assuming that WFs at the very upstream portion of the aperture are not affected by the shock, different tilts were added to each selected WF such that WFs were forced to be zeros for the first five spatial points at the very upstream portion of the aperture; results are re-plotted in Fig. 19, right plot. At time $T1 = -0.9$, the WF over the aperture is essentially zero, showing no visible signs of the shock. At time $T2 = -0.25$, a weak shock appears near $\alpha = 86.2$ deg and the WF exhibits a linear increase downstream of the shock. The shock is the strongest (by definition of the

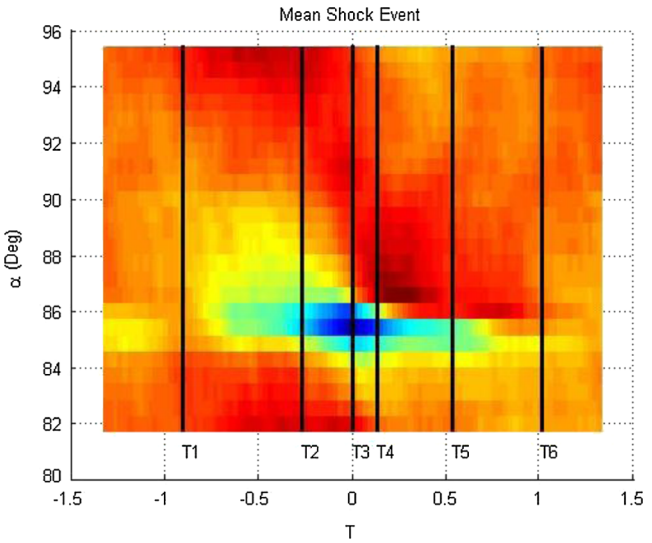

Fig. 18 Conditionally averaged WF data to produce an average shock event.

conditionally averaged procedure) at $T3 = 0$, also with the linearly increasing WF downstream of it. Shortly after the shock reaches its maximum strength at $T4 = 0.13$, the shock starts decreasing in its strength and moving upstream; the WF downstream of the shock also grows less, compared to the time instant T3. At the moment $T5 = 0.5$, the shock moves further upstream with even more decreased intensity; the WF essentially stays unchanged downstream of the shock. Finally, at $T6 = 0.9$, the shock disappears and the WF is again almost flat across the aperture.

Defining the shock strength as OPD jump across it, ΔOPD, the shock strength and its relative position on the turret are plotted in Fig. 20, left plot. Before providing a physical explanation of the observed shock behavior, recall that for low subsonic speeds, the pressure is the lowest and therefore the speed is the highest around the viewing angle of 85 deg[2]. If flow is subsonic everywhere around the turret, the flow speed decreases downstream of 85 deg. Thus, the subsonic flow is similar to the flow in the convergent-divergent nozzle, where the location of maximum velocity at 85 deg serves as the throat for the flow on top of the turret. If the incoming speeds is increased until a critical mach number of $M = 0.55$, the flow near 85 deg reaches the sonic speed.[2] If the incoming speed is slightly larger than the critical Mach number, which is $M = 0.65$ for the presented data, the flow is still subsonic upstream of the sonic throat at $\alpha = 85$ deg. Remember that the fluidic surface around the turret is not fixed, but experiences temporal-spatial changes due to the evolving boundary layer and the separated region downstream of the turret. Let us say that at the moment T1 the flow reaches the sonic speed at 85 deg. It becomes supersonic for a short distance downstream and then, due to the fluidic flow shape, becomes subsonic again, as schematically shown in Fig. 20, right. If at some moment T2 the supersonic region increases, it starts forming a small shock near the turret surface some distance downstream of the sonic throat. The velocity before the shock is at a maximum, corresponding to the most negative OPD value; after the shock, density and OPD increase sharply. When at the moment T3 shock gained enough strength, it will cause a premature separation forming immediately downstream of it. The increased separation bubble increases the local fluidic curvature, resulting in reduction of the streamwise velocity and pressure gradient, reduction in the pressure downstream of the shock and forcing the shock to move upstream at the moment T4. When the shock approaches the sonic line at the moment T5, the shock intensity is decreased and the shock eventually disappears at the moment T6, leaving the flow subsonic everywhere on top of the turret. Then the proposed scenario repeats itself, creating a recurrent pattern of emerging and

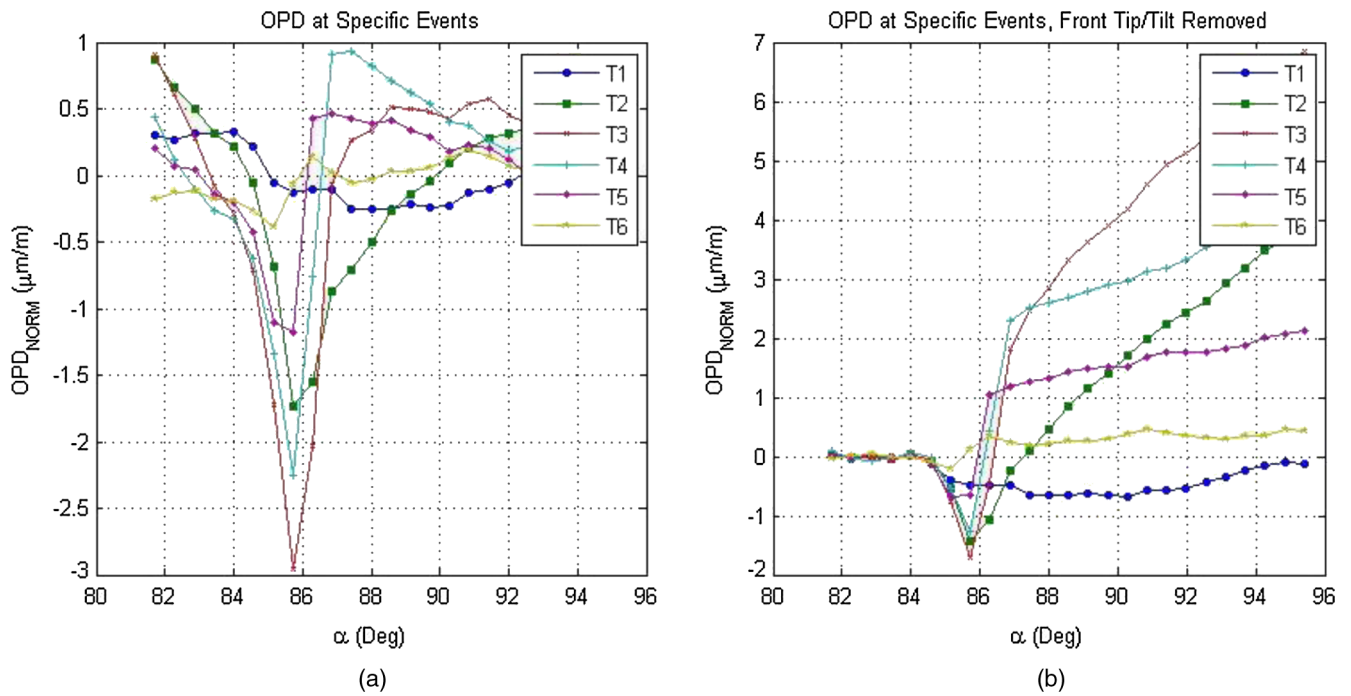

Fig. 19 Tilt-removed (a) and tilt-corrected (b) one-dimensional streamwise WFs at selected times, denoted in Fig. 14.

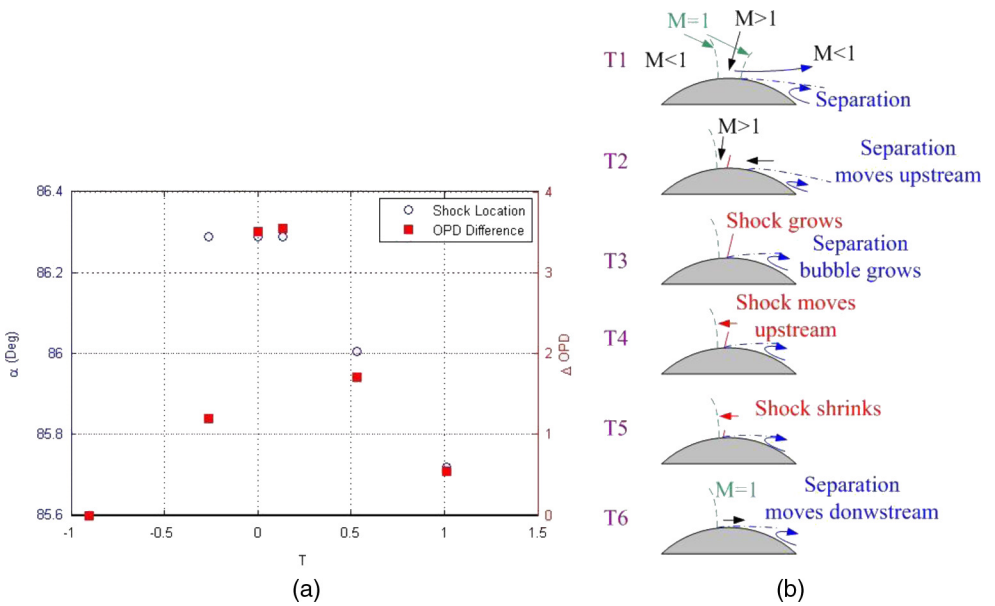

Fig. 20 (a) The shock strength, ΔOPD_{NORM}, and the shock location at different times centered around the maximum shock strength. (b) proposed physical mechanism of the shock temporal evolution.

disappearing shocks. As a final note, the similar shock-evolving mechanism was observed in the shock-induced separation on the wall of a slightly over-expended supersonic nozzle.[14]

The proposed physical mechanism of the shock dynamics also explains the somewhat surprising relatively slow shock motion, which is on the order of several characteristic turret times, D/U_∞. As it was shown before, the shock motion depends on the size and motion of the large separation region downstream of the turret, and it takes several characteristic turret times to change this global flow feature around the turret. Additional cross-correlation measurements between the local shock dynamics and the global separated region are needed to investigate and improve the proposed mechanism.

4 Conclusions

Using the AAOL, WF measurements were performed for both a hemisphere-on-cylinder turret and a hemisphere-only turret. Additionally, both conformal and flat windows were tested, and measurements were obtained at both subsonic and transonic velocities. Through the use of slewing maneuvers, measurements were taken over a large range of viewing angles to allow rapid mapping of the aero-optical performance of the turret in different configurations. The aero-optical environment was characterized through the computation of OPD_{RMS} and the standard deviation of OPD_{RMS}, Σ, at each viewing angle. Additionally, shock dynamics were investigated for a weak shock forming upstream of the turret apex in the transonic case.

The hemisphere-only turret mostly exhibits the same general flow features as the hemisphere-only turret. The separation bubble due to the presence of the flat window and the separation point for the wake remain unchanged from the full hemisphere-on-cylinder turret. These effects are dependent only on local geometry changes, and thus are mostly unaffected by the turret height. For $\alpha < 80$ deg, the hemisphere-only turret exhibits lower OPD_{RMS} values as a result of a smaller boundary layer on the turret. In the separated wake region, $\alpha > 110$–120 deg, OPD_{RMS} values are also lower for the hemisphere-only turret as the reduced profile results in a smaller, less turbulent wake. At high Els $\beta > 80$ deg, both the hemisphere-only turret and the hemisphere-on cylinder turret exhibit reduced OPD_{RMS} values as the aperture looks through the two horn vortices of the wake. However, the hemisphere-only turret has larger OPD_{RMS} in this range as the reduced profile results in the horn vortices being closer to the aperture than with the full turret.

In the transonic regime, the same trends hold: optical performance features due to local geometry remain unchanged while those dependent on global flow features are altered. Both exhibit an increase in OPD_{RMS} for 80 deg $< \alpha <$ 100 deg, due to the presence of the weak shock and for $\alpha >$ 110 deg due to a shock-related, prematurely tripped, and, therefore, larger turbulent wake. For the hemisphere-only turret, OPD_{RMS} values are again smaller in the wake region than for the full turret, as the turret wake is still smaller in this flow regime. Again, for both geometries, separation occurs at a smaller α in the transonic regime.

The spread in instantaneous OPD_{RMS} was shown to be approximately proportional to the time-mean value of OPD_{RMS}, $\Sigma \approx 0.28RMS_{RMS}$. Since the spatial OPD-distribution was found to be Gaussian, this relationship can be used to predict the probability distribution of the far-field Strehl Ratio. Given a far-field intensity threshold, the relative duration of intensity drop-outs, and, for communication applications, potential data-losses, can be predicted.

The dynamics of the weak shock that occurs near the top of the turret in the transonic regime at $M = 0.65$ were investigated. The dynamics of the shock, as well as the extent of its presence on the turret, was found to be unsteady at these speeds. The shock results from the flow becoming locally supersonic shortly downstream of the point of minimum c_p on the turret, at $\alpha = 85$ deg. As the shock grows in strength, a separation bubble appears downstream of it, with the increased recirculating flow pushing the shock forward towards the sonic line. As the shock reaches the sonic line, it dissipates as the flow is no longer supersonic.

Future work will include the study of flow control devices to improve the aero-optical environment about the hemisphere-on-cylinder turret. Additionally, study of the transonic flow regime will be expanded up to freestream Mach numbers of 0.85. This will allow the study of the evolution of shocks on the turret as a function of Mach number.

Acknowledgments

This work was funded by the High Energy Laser—Joint Technology Office (HEL-JTO) and administered through the Air Force Office for Scientific Research (AFOSR) under grant number FA9550-07-1-0574. The US government is authorized to reproduce and distribute reprints for government purposes notwithstanding any copyright notation thereon.

References

1. M. Wang, A. Mani, and S. Gordeyev, "Physics and computation of aero-optics," *Annu. Rev. Fluid Mech.* **44**, 299–321 (2012).
2. S. Gordeyev and E. Jumper, "Fluid dynamics and aero-optics of turrets," *Prog. Aerospace Sciences.* **46**(8), 388–400 (2010).
3. R. M. Rennie, G. Crahan, and E. Jumper, "Aerodynamic design of an aircraft-mounted pod for improved aero-optic performance," in *AIAA Aerospace Sciences Meeting*, Orlando, Florida (2010).
4. E. Jumper, M. Zenk, S. Gordeyev, and D. Cavalieri, "The Airborne Aero-Optics Laboratory, AAOL," *Proc. SPIE* **8395**, 839507 (2012).
5. M. R. Whiteley, D. J. Goorskey, and R. Drye, "Aero-optical jitter estimation using higher-order wavefronts," *Proc. SPIE* **8395**, 83950E (2012).
6. C. Porter, S. Gordeyev, M. Zenk, and E. Jumper, "Flight measurements of aero-optical distortions from a flat-windowed turret on the Airborne Aero-Optics Laboratory (AAOL)," in *AIAA*, Honolulu, Hawaii (2011).
7. A. E. Smith, S. Gordeyev, and E. Jumper, "Recent measurements of aero-optical effects caused by subsonic boundary layers," *Proc. SPIE* **8395**, 83950C (2012).
8. J. Cress, "Optical aberrations caused by coherent structures in a subsonic, compressible, turbulent boundary layer," Ph. D. Thesis, University of Notre Dame (2010).
9. N. DeLucca, S. Gordeyev, and E. Jumper, "Aero-optical environment around turrets at forward-viewing angles," to be presented at *AIAA Aerospace Sciences Meeting*, Grapevine, Texas (7–10 January 2013).
10. S. Gordeyev, J. A. Cress, E. Jumper, and A. B. Cain, "Aero-optical environment around a cylindrical turret with a flat window," *AIAA J.* **49**(2), 308–315 (2011).
11. T. S. Ross, "Limitations and applicability of the Maréchal approximation," *App. Opt.* **48**(10), 1812–1818 (2009).
12. S. Gordeyev, J. Cress, and E. Jumper, "Far-field intensity drop-outs caused by turbulent boundary layers," presented at *Beam Control Conference*, DEPS, Orlando, Fl. (23–26 May 2011).
13. D. J. Goorskey, "Spatial and temporal characterization of AAOL flight test data," *Proc. SPIE* **8395**, 839509 (2012).
14. B. J. Olson and S. K. Lele, "Large-eddy simulation of an over-expanded planar nozzle," in *AIAA*, Honolulu, Hawaii (2011).

Nicholas De Lucca is a fourth-year graduate student at the University of Notre Dame. He received double BS from the University of Minnesota-Twin Cities, Minnesota, in Aerospace Engineering and Astrophysics. He currently pursues research with the Notre Dame Aero-Optics Group and has been working directly with the Airborne Aero-Optics Laboratory (AAOL) Program for more than a year. Personal research topics include aero-optical and fluid dynamical properties of turrets, with an emphasis on measurement and mitigation of aero-optical and aero-mechanical beam jitter.

Biographies and photographs of the other authors are not available.